Mathematics of Sea Ice

K. M. Golden

Department of Mathematics
University of Utah

1 Introduction

Among the large-scale transformations of the Earth's surface that are apparently due to global warming, the sharp decline of the summer Arctic sea ice pack is probably the most dramatic. For example, the area of the Arctic Ocean covered by sea ice in September of 2012 was less than half of its average over the 1980's and 1990's. While global climate models generally predict declines in the polar sea ice packs over the 21st century, these precipitous losses have significantly outpaced most projections. Here we will show how mathematics is being used to better understand the role of sea ice in the climate system and improve projections of climate change. In particular, we will focus on how mathematical models of composite materials and statistical physics are being used to study key sea ice structures and processes, and represent sea ice more rigorously in global climate models. Also, we will briefly discuss these climate models as systems of partial differential equations (PDEs) solved using computer programs with millions of lines of code, on some of the world's most powerful computers, with particular focus on their sea ice components.

1.1 Sea Ice and the Climate System

Sea ice is frozen ocean water, which freezes at a temperature of about -1.8° C, or 28.8° F. As a material, sea ice is quite different from the glacial ice in the world's great ice sheets covering Antarctica and Greenland. When salt water freezes, the result is a composite of pure ice with inclusions of liquid brine, air pockets, and solid salts. As the temperature of sea ice increases, the porosity or volume fraction of brine increases. The brine inclusions in sea ice host extensive algal and bacterial communities which are essential for supporting life in the polar oceans. For example, krill feed on the algae, and in turn support fishes, penguins, seals, and Minke whales, and up the food chain to the top predators – killer whales, leopard seals, and polar bears. The brine microstructure also facilitates the flow of salt water through sea ice, which mediates a broad range of processes, such as the growth and decay of seasonal ice, the evolution of ice pack reflectance, and biomass build-up.

As the boundary between the ocean and atmosphere in the polar regions of Earth, sea ice plays a critical role as both a leading indicator of climate change, and as a key player in the global climate system. Roughly speaking, most of the solar radiation which is incident on snow-covered sea ice is reflected, while most of the solar radiation which is incident on darker sea water is absorbed. The sea ice packs serve as part of Earth's polar refrigerator, cooling it and protecting it from absorbing too much heat from sunlight. The ratio of reflected sunlight to incident sunlight is called albedo. While the albedo of snow-covered ice is close to 1 (larger than 0.8), the albedo of sea water is close to zero (less than 0.1).

Ice-albedo feedback. As warming temperatures melt more sea ice over time, fewer bright surfaces are available to reflect sunlight, more heat escapes from the ocean to warm the atmosphere, and the ice melts further. As more ice is melted, the albedo of the polar oceans is lowered, leading to more solar absorption and warming, which in turn leads to more melting, in a positive feedback loop. It is believed that this so-called *ice-albedo feedback* has played an important role in the recent dramatic declines in summer Arctic sea ice extent.

Thus even a small increase in temperature can lead to greater warming over time, making the polar regions the most sensitive areas to climate change on Earth. Global warming is *amplified* in the polar regions. Indeed, global climate models consistently show amplified warming in the high latitude Arctic, although the magnitude varies considerably across different models. For example, the average surface air temperature at the North Pole by the end of the 21^{st} century is predicted to rise by a factor of about 1.5 to 4 times the predicted increase in global average surface air temperature.

While global climate models generally predict declines in sea ice area and thickness, they have significantly underestimated the recent dramatic losses observed in summer Arctic sea ice. Im-

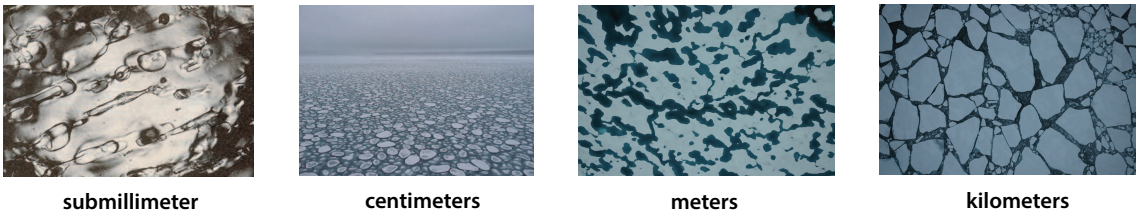

Figure 1: Sea ice exhibits composite structure on length scales over many orders of magnitude. From left to right: the sub-millimeter scale brine inclusions in sea ice; pancake ice in the Southern Ocean with microstructural scale on the order of tens of centimeters; melt ponds on the surface of Arctic sea ice with meter scale microstructure; ice floes in the Arctic Ocean on the kilometer scale.

proving projections of the fate of Earth's sea ice cover and its ecosystems depends on a better understanding of important processes and feedback mechanisms. For example, during the melt season the Arctic sea ice cover becomes a complex, evolving mosaic of ice, melt ponds, and open water. The albedo of sea ice floes is determined by melt pond evolution. Drainage of the ponds, with a resulting increase in albedo, is largely controlled by the fluid permeability of the porous sea ice underlying the ponds. As ponds develop, ice–albedo feedback enhances the melting process. Moreover, this feedback loop is the driving mechanism in mathematical models developed to address the question of whether we have passed a so-called *tipping point* or *critical threshold* in the decline of summer Arctic sea ice. Such studies often focus on the existence of a saddle node bifurcation in dynamical system models of sea ice coverage of the Arctic Ocean. In general, sea ice albedo represents a significant source of uncertainty in climate projections and a fundamental problem in climate modeling.

Multiscale structure of sea ice. One of the fascinating, yet challenging aspects of modeling sea ice and its role in global climate is the sheer range of relevant length scales of structure, over ten orders of magnitude from the submillimeter scale to hundreds of kilometers. In Figure 1 we show examples of sea ice structure illustrating such a range of scales. Modeling sea ice on a large scale depends on some understanding of the physical properties of sea ice at the scale of individual floes, and even on the submillimeter scale since the brine phase in sea ice is such a key *determinant* of its bulk physical properties. Today's climate models challenge the most powerful super computers to their fullest capacity. However, even the largest computers still limit the horizontal resolution to tens of kilometers and require clever approximations and parameterizations to model the basic physics of sea ice. One of the central themes of this article is how to use information on smaller scales to predict behavior on larger scales. We observe that this central problem of climate science shares commonality with the key challenges, for example, in theoretical computations of the effective properties of composites.

Here we'll explore some of the mathematics used in studying sea ice and its role in the climate system, particularly through the lens of sea ice albedo and processes related to its evolution.

2 Global Climate Models and Sea Ice

Global climate models, also known as General Circulation Models (GCM's), are systems of PDEs derived from the basic laws of physics, chemistry, and fluid motion. They describe the state of the ocean, ice, atmosphere, and land, as well as their interactions. The equations are solved on very powerful computers using 3-dimensional grids of the air-ice-ocean-land system, with horizontal grid sizes on the order of tens of kilometers. Consideration of general climate models will take us too far afield, but here we will briefly consider the sea ice components of these large scale models.

The polar sea ice packs consist primarily of open water, thin first-year ice, thicker multiyear ice, and pressure ridges created by ice floes col-

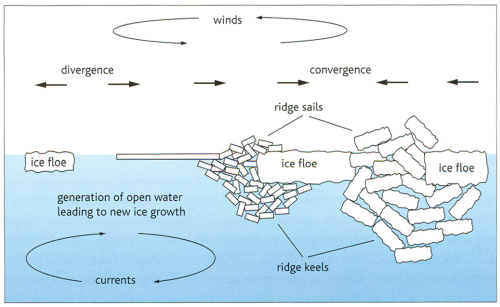

Figure 2: Different factors contributing to the evolution of the ice thickness distribution $g(h, x, t)$.

liding with each other. The dynamic and thermodynamic characteristics of the ice pack depend largely on how much ice is in each thickness range. One of the most basic problems in sea ice modeling is thus to describe the evolution of the ice thickness distribution (ITD) in space and time. The ITD $g(x, t, h)dh$ is defined (informally) as the fractional area covered by ice in the thickness range $(h, h + dh)$ at a given time t and location x. The fundamental equation controlling the evolution of the ITD, which is solved numerically in sea ice models, is

$$\frac{\partial g}{\partial t} = -\nabla \cdot (g\mathbf{u}) - \frac{\partial}{\partial h}(\beta g) + \Psi$$

where $\mathbf{u}$ is the horizontal ice velocity, β is the rate of thermodynamic ice growth, and Ψ is a ridging redistribution function which accounts for changes in ice thickness due to ridging and mechanical processes, as illustrated in Figure 2.

The momentum equation, or Newton's second law for sea ice, can be deduced by considering the forces on a single floe, including interactions with other floes,

$$m\frac{D\mathbf{u}}{Dt} = \nabla \cdot \boldsymbol{\sigma} + \boldsymbol{\tau}_a + \boldsymbol{\tau}_w - m\alpha\mathbf{n} \times \mathbf{u} - mg\nabla H,$$

where each term has units of force per unit area of the sea ice cover, m is the combined mass of ice and snow per unit area, $\boldsymbol{\tau}_a$ and $\boldsymbol{\tau}_w$ are wind and ocean stresses, and $\frac{D}{Dt} = \frac{\partial}{\partial t} + \mathbf{u} \cdot \nabla$ is the material or convective derivative. This is a two dimensional equation, obtained by integrating the 3D equation through the thickness of the ice in the vertical direction.

The strength of the ice is represented by the internal stress tensor σ_{ij}. The other two terms on the right hand side are, in order, stresses due to Coriolis effects and the sea surface slope, where $\mathbf{n}$ is a unit normal vector in the vertical direction, α is the Coriolis parameter, H describes the sea surface, and in this equation g is the acceleration due to gravity.

The temperature field $T(x, t)$ inside the sea ice (and snow layer), which couples to the ocean below and the atmosphere above through appropriate boundary conditions, satisfies an advection diffusion equation,

$$\frac{\partial T}{\partial t} = \nabla \cdot (D(T)\,\nabla T) - \mathbf{v} \cdot \nabla T,$$

where $D = K/\rho C$ is the thermal diffusivity of sea ice, K is its thermal conductivity, ρ its bulk density, C the specific heat, and $\mathbf{v}$ is an averaged brine velocity field in the sea ice.

The bulk properties of low Reynolds number flow of brine of viscosity η through sea ice can be related to the geometrical properties of the porous brine microstructure using **homogenization theory**. The volume fractions of brine and ice are ϕ and $1 - \phi$. The local velocity and pressure fields in the brine satisfy the Stokes equations for incompressible fluids, where the length scale of the microstructure (for example, the period in periodic media) is ϵ. Under appropriate assumptions, in the homogenization limit as $\epsilon \longrightarrow 0$, the averaged velocity $\mathbf{v}(x)$ and pressure $p(x)$ satisfy Darcy's law and the incompressibility condition,

$$\mathbf{v} = -\frac{1}{\eta}\,\mathbf{k}\,\nabla p, \qquad \nabla \cdot \mathbf{v} = 0. \tag{1}$$

Here, $\mathbf{k}$ is the permeability tensor, with vertical component $\mathrm{k}_{zz} = k$ in units of m^2. The permeability $\mathbf{k}$ is an example of an *effective* or *homogenized parameter*. The existence of the homogenized limits $\mathbf{v}, \mathbf{k}$, and p in (1) can be proven under broad assumptions, such as for media with inhomogeneities that are periodic or have translation invariant statistics.

Obtaining quantitative information on $\mathbf{k}$ or other effective transport coefficients such as electrical or thermal conductivity and how they depend on, say, the statistical properties of the microstructure, is a central problem in the theory

of composites. A broad range of techniques have been developed to obtain rigorous bounds, approximate formulas and general theories of effective properties of composite and inhomogeneous media, in terms of partial information about the microstructure. This problem is, of course, quite similar in nature to the fundamental questions of calculating bulk properties of matter from information on molecular interactions – central to statistical mechanics.

We note that it is also the case that one of the fundamental challenges of climate modeling is how to rigorously account for sub-grid scale processes and structures in models whose grid size is far greater than the scale of relevant phenomena. For example, obviously it is not realistic to account for every detail of the sub-millimeter scale brine microstructure in sea ice in a GCM! However, the volume fraction and connectedness properties of the brine phase control whether or not fluid can flow through the ice. The *on–off switch* for fluid flow in sea ice, known as the *rule of fives* (see below), in turn controls such critical processes as melt pond drainage, snow ice formation (where sea water percolates upward, floods the snow layer on the sea ice surface and subsequently freezes), the evolution of salinity profiles, and nutrient replenishment. It is the homogenized transport coefficient – the effective fluid permeability – which is incorporated into sea ice and climate models to account for these and related physical and biogeochemical processes. This effective coefficient is a well defined parameter (under appropriate assumptions about the microstructure) which captures the relevant microstructural transitions and determines how a number of sea ice processes evolve. In this example, we will see that rigorous mathematical methods can be employed to analyze effective sea ice behavior on length scales much greater than the submillimeter scale of the brine inclusions.

3 Mathematics of Composites

Here we give a brief overview of some of the mathematical models and techniques that are used in studying the effective properties of sea ice.

3.1 Percolation Theory

Percolation theory was initiated in 1957 with the introduction of a simple lattice model to study the flow of air through permeable sandstones used in miner's gas masks. In subsequent decades, this theory has been used to successfully model a broad array of disordered materials and processes, including flow in porous media like rocks and soils, doped semiconductors, and various types of disordered conductors like piezoresistors, thermistors, radar absorbing composites, carbon nanotube composites, and polar firn. The original percolation model and its generalizations have been the subject of intensive theoretical investigations, particularly in the physics community. One reason for the broad interest in the percolation model is that it is perhaps the simplest, purely probabilistic model which exhibits a type of phase transition.

The simplest form of the lattice percolation model is defined as follows. Consider the $d-$dimensional integer lattice $\mathbb{Z}^d$, and the square or cubic network of bonds joining nearest neighbor lattice sites. We assign to each bond a conductivity $\sigma_0 > 0$ (not to be confused with the stress tensor above) with probability p, meaning it is open (black), and a conductivity 0 with probability $1-p$, meaning it is closed. Two examples of lattice configurations are shown in Figure 3, with $p = 1/3$ in (a) and $p = 2/3$ in (b). Groups of connected open bonds are called *open clusters*. In this model there is a critical probability p_c, $0 < p_c < 1$, called the *percolation threshold*, at which the average cluster size diverges and an infinite cluster appears. For the two dimensional bond lattice $p_c = 1/2$. For $p < p_c$ the density of the infinite cluster $P_\infty(p)$ is 0, while for $p > p_c$, $P_\infty(p) > 0$ and near the threshold,

$$P_\infty(p) \sim (p - p_c)^\beta, \qquad p \to p_c^+,$$

where β is a universal critical exponent, that is, it depends only on dimension and not on the details of the lattice. Let $x, y \in \mathbb{Z}^d$ and $\tau(x, y)$ be the probability that x and y belong to the same open cluster. The correlation length $\xi(p)$ is the mean distance between points on an open cluster, and is a measure of the linear size of finite clusters. For $p < p_c$, $\tau(x, y) \sim e^{-|x-y|/\xi(p)}$, and $\xi(p) \sim (p_c - p)^{-\nu}$ diverges with a universal critical exponent

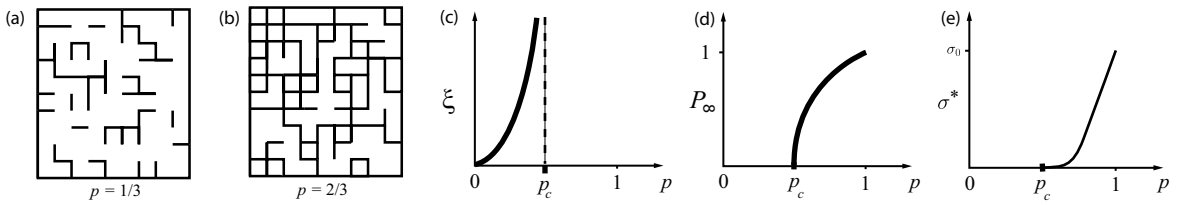

Figure 3: The two dimensional square lattice percolation model below its percolation threshold of $p_c = 1/2$ in (a) and above it in (b). (c) Divergence of the correlation length as p approaches p_c. The infinite cluster density of the percolation model is shown in (d), and the effective conductivity is shown in (e).

ν as $p \to p_c^-$, as shown in Figure 3 (c).

The effective conductivity $\sigma^*(p)$ of the lattice, now viewed as a random resistor (or conductor) network, defined via Kirchoff's laws, vanishes for $p < p_c$ like $P_\infty(p)$ since there are no infinite pathways, as shown in Figure 3 (e). For $p > p_c$, $\sigma^*(p) > 0$, and near p_c,

$$\sigma^*(p) \sim \sigma_0(p - p_c)^t, \qquad p \to p_c^+,$$

where t is the conductivity critical exponent, with $1 \le t \le 2$ in $d = 2, 3$, and numerical values $t \approx 1.3$ in $d = 2$ and $t \approx 2.0$ in $d = 3$. Consider a random pipe network with effective fluid permeability $k^*(p)$ exhibiting similar behavior $k^*(p) \sim k_0(p - p_c)^e$, where e is the permeability critical exponent, with $e = t$ for lattices Both t and e are believed to be universal − they depend only on dimension and not on the type of lattice. Continuum models, like the so-called *Swiss cheese model*, can exhibit non–universal behavior with exponents different from the lattice case and $e \neq t$.

3.2 Analytic Continuation and Spectral Measures

Homogenization is where one seeks to find a homogeneous medium which behaves macroscopically the same as a given inhomogeneous medium. The methods are focused on finding the effective properties of inhomogeneous media such as composites. We will see that the *spectral measure* in a Stieltjes integral representation for the effective parameter provides a powerful tool for upscaling geometrical information about a composite into calculations of effective properties.

We now briefly describe the *analytic continuation method* (ACM) for studying the effective transport properties of composite materials. This method has been used to obtain rigorous bounds on effective transport coefficients of two-component and multicomponent composite materials. The bounds follow from the special analytic structure of the representations for the effective parameters, and partial knowledge of the microstructure, such as the relative volume fractions of the phases in the case of composite media. The ACM was later adapted to treating the effective diffusivity of passive tracers in incompressible fluid velocity fields.

We consider the effective complex permittivity tensor $\boldsymbol{\epsilon}^*$ of a two-phase random medium, although the method applies to any classical transport coefficient. Here, $\epsilon(\mathbf{x}, \omega)$ is a (spatially) stationary random field in $\mathbf{x} \in \mathbb{R}^d$ and $\omega \in \Omega$, where Ω is the set of all geometric realizations of the medium, which is indexed by the parameter ω representing one particular realization, and the underlying probability measure P is compatible with stationarity.

As in sea ice, we assume we are dealing with a two-phase locally isotropic medium, so that the components ϵ_{jk} of the local permittivity tensor $\boldsymbol{\epsilon}$ satisfy $\epsilon_{jk}(x, \omega) = \epsilon(x, \omega)\delta_{jk}$, where δ_{jk} is the Kronecker delta and

$$\epsilon(x, \omega) = \epsilon_1\chi_1(x, \omega) + \epsilon_2\chi_2(x, \omega). \qquad (2)$$

Here, ϵ_j is the *complex* permittivity for medium $j = 1, 2$ and $\chi_j(x, \omega)$ is its characteristic function, equaling 1 for $\omega \in \Omega$ with medium j at $\mathbf{x}$, and 0 otherwise, with $\chi_2 = 1 - \chi_1$.

When the wavelength is much larger than the scale of the composite microstructure, the propagation properties of an electromagnetic wave in a given composite medium are determined by the

Figure 4: Ocean swells propagating through a vast field of pancake ice in the Southern Ocean off the coast of East Antarctica (photo by K. M. Golden). These long waves do not "see" the individual floes, whose diameters are on the order of tens of centimeters. The bulk wave propagation characteristics are largely determined by the homogenized or effective rheological properties of the pancake/frazil conglomerate on the surface.

quasi-static limit of Maxwell's equations

$$\nabla \times \mathbf{E} = 0, \quad \nabla \cdot \mathbf{D} = 0, \tag{3}$$

where $\mathbf{E}(\mathbf{x}, \omega)$ and $\mathbf{D}(\mathbf{x}, \omega)$ are stationary electric and displacement fields, respectively, related by the local constitutive equation $\mathbf{D}(\mathbf{x}) = \epsilon(\mathbf{x})\mathbf{E}(\mathbf{x})$, and $\mathbf{e}_k$ is a standard basis vector in the k^{th} direction. The electric field is assumed to be unit strength on average, with $\langle \mathbf{E} \rangle = \mathbf{e}_k$, where $\langle \cdot \rangle$ denotes ensemble averaging over Ω or spatial average over all of $\mathbb{R}^d$. The effective complex permittivity tensor $\boldsymbol{\epsilon}^*$ is defined by

$$\langle \mathbf{D} \rangle = \boldsymbol{\epsilon}^* \langle \mathbf{E} \rangle. \tag{4}$$

which is an homogenized version of the local constitutive relation $\mathbf{D} = \epsilon \mathbf{E}$.

For simplicity, we focus on one diagonal coefficient $\epsilon^* = \epsilon^*_{kk}$, with $\epsilon^* = \langle \epsilon \mathbf{E} \cdot \mathbf{e}_k \rangle$. By the homogeneity of $\epsilon(\mathbf{x}, \omega)$ in (2), ϵ^* depends on the contrast parameter $h = \epsilon_1/\epsilon_2$ and we define $m(h) = \epsilon^*/\epsilon_2$, which is a Herglotz function that maps the upper half h–plane to the upper half plane, and is analytic off $(-\infty, 0]$.

The key step in the method is obtaining a Stieltjes integral representation for ϵ^*. This integral representation arises from a resolvent representation of the electric field $\mathbf{E} = s(sI - \Gamma\chi_1)^{-1}\mathbf{e}_k$, where $\Gamma = \nabla(\Delta^{-1})\nabla\cdot$ acts as a projection from $L^2(\Omega, P)$ onto the Hilbert space of curl-free random fields, and Δ^{-1} is based on convolution with the free space Green's function for the Laplacian $\Delta = \nabla^2$. Consider the function $F(s) = 1 - m(h), s = 1/(1-h)$, which is analytic off $[0, 1]$ in the s-plane. Then writing $F(s) = \langle \chi_1 [(sI - \Gamma\chi_1)^{-1} e_k] \cdot e_k \rangle$ yields

$$F(s) = \int_0^1 \frac{d\mu(\lambda)}{s - \lambda}, \tag{5}$$

where $\mu(d\lambda) = \langle \chi_1 Q(d\lambda)\mathbf{e}_k \cdot \mathbf{e}_k \rangle$ is a positive *spectral measure* on $[0, 1]$ and $Q(d\lambda)$ is the (unique) projection valued measure associated with the bounded, self-adjoint operator $\Gamma\chi_1$.

Equation (5) is based on the spectral theorem for the resolvent of the operator $\Gamma\chi_1$. It provides a Stieltjes integral representation for the effective complex permittivity ϵ^* which separates the component parameters in s from the complicated geometrical information contained in the measure μ. (Extensions of (5) to multicomponent media with $\epsilon = \epsilon_1\chi_1 + \epsilon_2\chi_2 + \epsilon_3\chi_3 + \cdots + \epsilon_n\chi_n$ involve several complex variables.) Information about the geometry enters through the moments

$$\mu_n = \int_0^1 \lambda^n d\mu(\lambda) = \langle \chi_1 [(\Gamma\chi_1)^n \mathbf{e}_k] \cdot \mathbf{e}_k \rangle,$$

$n = 0, 1, 2, \ldots$. For example, the mass μ_0 is given by $\mu_0 = \langle \chi_1 \mathbf{e}_k \cdot \mathbf{e}_k \rangle = \langle \chi_1 \rangle = \phi$, where ϕ is the volume or area fraction of material of phase 1, and $\mu_1 = \phi(1-\phi)/d$ if the material is statistically isotropic. In general, μ_n depends on the $(n+1)$–point correlation function of the medium.

Computing the spectral measure μ for a given composite microstructure first involves discretizing a two phase image of the composite into a square lattice filled with 1's and 0's corresponding to the two phases. Then the key operator $\Gamma\chi_1$, which depends on the geometry via χ_1, becomes a self adjoint matrix. The spectral measure may be calculated directly from the eigenvalues and eigenvectors of this matrix.

4 Applications to Sea Ice

4.1 Percolation Theory

Given a sample of sea ice at temperature T in degrees Celsius and bulk salinity S in parts

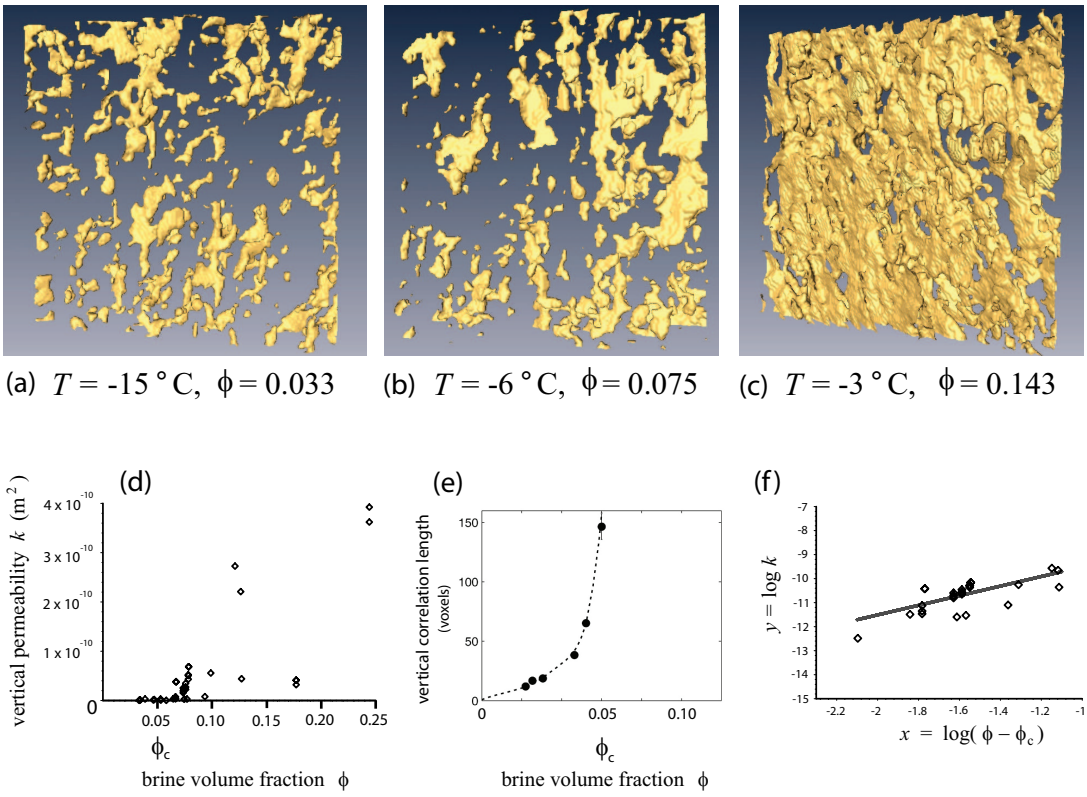

Figure 5: X-ray CT volume rendering of brine layers within a lab-grown sea-ice single crystal with S = 9.3 ppt. The (non-collocated) 8 × 8 × 2 mm sub-volumes (a)–(c) illustrate a pronounced change in the micro-scale morphology and connectivity of the brine inclusions during warming. (d) Data for the vertical fluid permeability k taken *in situ* on Arctic sea ice, displayed on a linear scale. (e) Divergence of the brine correlation length in the vertical direction as the percolation threshold is approached from below. (f) Comparison of Arctic permeability data in the critical regime (25 data points) with percolation theory in (7). In logarithmic variables the predicted line has the equation $y = 2\,x - 7.5$, while a best fit of the data yields $y = 2.07\,x - 7.45$, assuming $\phi_c = 0.05$.

per thousand (ppt), the brine volume fraction ϕ is given (approximately) by the equation of Frankenstein and Garner,

$$\phi = \frac{S}{1000}\left(\frac{49.185}{|T|} + 0.532\right). \qquad (6)$$

As temperature increases for fixed salinity, the volume fraction ϕ of liquid brine in the ice also increases. The inclusions become larger and more connected, as illustrated in Figure 5 (a)–(c), which shows images of the brine phase in sea ice (in gold) obtained from X-ray tomography scans of sea ice single crystals.

As the connectedness of the brine phase increases with rising temperature, the ease with which fluid can flow through sea ice – its fluid permeability – should increase as well. In fact, sea ice exhibits a *percolation threshold*, or critical brine volume fraction ϕ_c, or critical temperature T_c, below which columnar sea ice is effectively impermeable to vertical fluid fluid flow, and above which the ice is permeable, and increasingly so as temperature rises. This critical behavior of fluid transport in sea ice is illustrated in Figure 5 (d). The data on the vertical fluid permeability $k(\phi)$ display a rapid rise just above a threshold value of about $\phi_c \approx 0.05$ or 5%, similar to the conductivity (or permeability) in Figure 3 (e). This type of behavior is also displayed by data on brine drainage, with the effects of drainage

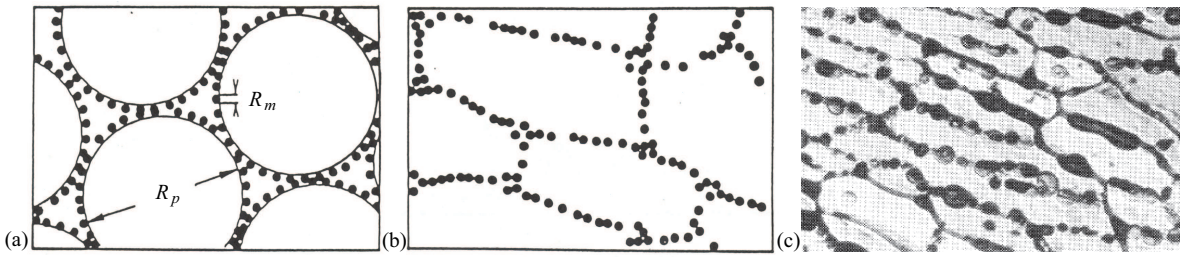

Figure 6: (a) A powder of large polymer spheres mixed with smaller metal spheres. (b) When the powder is compressed, its microstrucure is similar to that of sea ice in (c).

shutting down for brine volume fractions below about 5%. Roughly speaking, we can refer to this phenomenon as the *on–off switch* for fluid flow in sea ice. Through the Frankenstein–Garner relation in Equation 6, the critical brine volume fraction $\phi_c \approx 0.05$ corresponds to a critical temperature $T_c \approx -5°$C, for a typical salinity of 5 ppt. Thus, this important threshold behavior has become known as the *rule of fives*.

In view of this type of critical behavior, it is reasonable to try and find a percolation theoretic explanation. However, with $p_c \approx 0.25$ for the $d = 3$ cubic bond lattice, it was apparent that key features of the geometry of the brine microstructure in sea ice were being missed by lattices. The threshold $\phi_c \approx 0.05$ was identified with the critical probability in a continuum percolation model for compressed powders which exhibit microstructural characteristics similar to sea ice. The identification explained the rule of fives, as well as data on algal growth and snow-ice production. The compressed powders, shown in Figure 6, were used in the development of so-called *stealthy* or radar absorbing composites.

When we applied the compressed powder model to sea ice, we had no *direct* evidence that the brine microstructure undergoes a transition in connectedness at a critical brine volume fraction. This lack of evidence was due partly to the difficulty of imaging and quantitatively characterizing the brine inclusions in three dimensions, particularly the thermal evolution of their connectivity. Through X-ray computed tomography and pore structure analysis we have now analyzed critical behavior of the thermal evolution of brine connectedness in sea ice single crystals, over a temperature range from $-18°$ C to $-3°$ C. We have mapped three dimensional images of the pores and throats in the brine phase onto graphs of nodes and edges, and analyzed their connectivity as functions of temperature and sample size. Realistic network models of brine inclusions can be derived from porous media analysis of 3-D micro-tomography images. Using finite-size scaling techniques largely confirms the rule of fives, and that sea ice is a natural material that exhibits a strong anisotropy in percolation thresholds.

Now we consider the application of percolation theory to understanding the fluid permeability of sea ice. In the continuum, the permeability and conductivity exponents e and t can take non-universal values, and need not be equal, such as for the three dimensional Swiss cheese model. Continuum models have been studied by mapping to a lattice with a probability density $\psi(g)$ of bond conductances g. Non-universal behavior can be obtained when $\psi(g)$ is singular as $g \to 0^+$. However, for a lognormal conductance distribution arising from intersections of lognormally distributed inclusions, as in sea ice, the behavior is *universal*. Thus $e \approx 2$ for sea ice.

The permeability scaling factor k_0 for sea ice is estimated using *critical path analysis*. For media with g in a wide range, the overall behavior is dominated by a critical, *bottleneck* conductance g_c, the smallest conductance such that the critical path $\{g : g \geq g_c\}$ spans the sample. With most brine channel diameters between 1.0 mm and 1.0 cm, spanning fluid paths have a smallest, characteristic radius $r_c \approx 0.5$ mm, and we estimate k_0 by the pipe-flow result ${r_c}^2/8$. Thus

$$k(\phi) \sim 3\,(\phi - \phi_c)^2 \times 10^{-8}\ \mathrm{m}^2, \quad \phi \to \phi_c^+. \quad (7)$$

In Figure 5 (f), field data with ϕ in $[0.055, 0.15]$,

just above $\phi_c \approx 0.05$, are compared with (7), showing close agreement. The striking result that for sea ice, $e \approx 2$, the universal *lattice* value in three dimensions, is due to the general lognormal structure of the brine inclusion distribution function. The general nature of our results suggests that similar types of porous media, such as saline ice on extraterrestrial bodies, may also exhibit universal critical behavior.

4.2 Analytic Continuation

4.2.1 Bounds on the Effective Complex Permittivity

Bounds on ϵ^*, or $F(s)$, are obtained by fixing s in (5), varying over admissible measures μ (or admissible geometries), such as those that satisfy only

$$\mu_0 = \phi. \tag{8}$$

and finding the corresponding range of values of $F(s)$ in the complex plane. Two types of bounds on ϵ^* are obtained. The first bound R_1 assumes only that the relative volume fractions $p_1 = \phi$ and $p_2 = 1-p_1$ of the brine and ice are known, so that (8) is satisfied. In this case, the admissible set of measures forms a compact, convex set. Since (5) is a linear functional of μ, the extreme values of F are attained by extreme points of the set of admissible measures, which are the Dirac point measures of the form $p_1\delta_z$. The values of F must lie inside the circle $p_1/(s-z)$, $-\infty \le z \le \infty$, and the region R_1 is bounded by circular arcs, one of which is parametrized in the F–plane by

$$C_1(z) = \frac{p_1}{s-z}\,, \qquad 0 \le z \le p_2. \tag{9}$$

To display the other arc, it is convenient to use the auxiliary function

$$E(s) = 1 - \frac{\epsilon_1}{\epsilon^*} = \frac{1 - sF(s)}{s(1-F(s))}\,, \tag{10}$$

which is a Herglotz function like $F(s)$, analytic off $[0,1]$. Then in the E–plane, we can parametrize the other circular boundary of R_1 by

$$\hat{C}_1(z) = \frac{p_2}{s-z}\,, \qquad 0 \le z \le p_1. \tag{11}$$

In the ϵ^*–plane, R_1 has vertices $V_1 = \epsilon_1/(1-\hat{C}_1(0)) = (p_1/\epsilon_1 + p_2/\epsilon_2)^{-1}$ and $W_1 = \epsilon_2(1-C_1(0)) = p_1\epsilon_1 + p_2\epsilon_2$, and collapses to the interval

$$(p_1/\epsilon_1 + p_2/\epsilon_2)^{-1} \le \epsilon^* \le p_1\epsilon_1 + p_2\epsilon_2 \tag{12}$$

when ϵ_1 and ϵ_2 are real, which are the classical arithmetic (upper) and harmonic (lower) mean bounds, also called the elementary bounds. The complex elementary bounds (9) and (11) are optimal and can be attained by a composite of uniformly aligned spheroids of material 1 in all sizes coated with confocal shells of material 2, and vice versa. These arcs are traced out as the aspect ratio varies.

If the material is further assumed to be statistically isotropic, i.e., $\epsilon^*_{ik} = \epsilon^*\delta_{ik}$, then $\mu_1 = \phi(1-\phi)/d$ must be satisfied as well. A convenient way of including this information is to use the transformation,

$$F_1(s) = \frac{1}{p_1} - \frac{1}{sF(s)}\,. \tag{13}$$

The function $F_1(s)$ is, again, a Herglotz function which has the representation

$$F_1(s) = \int_0^1 \frac{d\mu^1(z)}{s-z}\,. \tag{14}$$

The constraint $\mu_1 = \phi(1-\phi)/d$ on $F(s)$ is then transformed to a restriction of only the mass, or zeroth moment μ^1_0 of μ^1, with

$$\mu^1_0 = p_2/p_1 d. \tag{15}$$

Applying the same procedure as for R_1 yields a region R_2, whose boundaries are again circular arcs. When ϵ_1 and ϵ_2 are real with $\epsilon_1 \ge \epsilon_2$, the region collapses to a real interval, whose endpoints are known as the Hashin–Shtrikman bounds. We remark that higher–order correlation information can be conveniently incorporated by iterating (13).

4.2.2 Inverse Homogenization

It has been shown that the spectral measure μ, which contains all geometrical information about a composite, can be uniquely reconstructed if measurements of the effective permittivity ϵ^* are available on an arc in the complex $s-$plane. If the component parameters depend on frequency ω (not to be confused with realizations of the random medium above), variation of ω in an interval

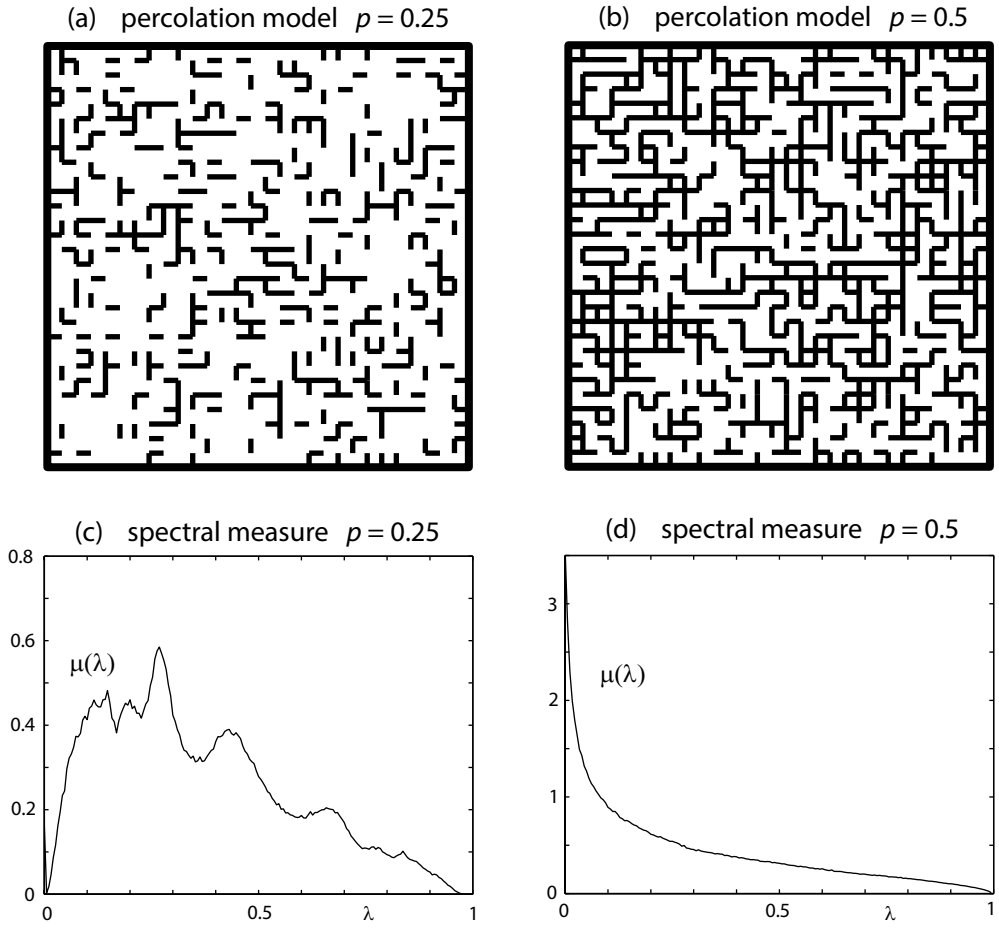

Figure 7: Realizations of the two dimensional lattice percolation model are shown in (a) and (b), and the corresponding spectral functions (averaged over 5000 random realizations) are shown in (c) and (d). In (c), there is a spectral gap around $\lambda = 1$, indicating the lack of long-range order or connectedness. The gap collapses in (d) when the percolation threshold of $p = p_c = 0.5$ has been reached, and the system exhibits long-range connectedness. Note the difference in vertical scale in the graphs in (c) and (d).

(ω_1, ω_2) gives the required data. Reconstructing μ can be reduced to an inverse potential problem. Indeed, $F(s)$ admits a representation through a logarithmic potential Φ of the measure μ,

$$F(s) = \frac{\partial \Phi}{\partial s}\,, \quad \Phi(s) = \int_0^1 \ln|s - z|\, d\mu(z), \quad (16)$$

where $\partial/\partial s = (\partial/\partial x - i\ \partial/\partial y)$ The potential Φ solves the Poisson equation $\Delta\Phi = -\rho$, where $\rho(z)$ is a density on $[0, 1]$. A solution to the forward problem is given by the Newtonian potential with $\mu(dz) = \rho(z)dz$. The inverse problem is to find $\rho(z)$ (or μ) given values of $\Phi, \partial\Phi/\partial n$, or $\nabla\Phi$. The inverse problem is extremely ill-posed and requires regularization to develop a stable numerical algorithm.

When frequency ω varies across the interval (ω_1, ω_2), the complex parameter s traces an arc $\mathcal{C}$ in the s-plane. Let A be the integral operator in (16), $A\mu = \frac{\partial}{\partial s}\int_0^1 \ln|s-\lambda|\ d\mu(\lambda)$, mapping the set of measures $\mathcal{M}[0, 1]$ on the unit interval onto the set of derivatives of complex potentials defined on a curve $\mathcal{C}$. To construct the solution we consider the problem of minimizing $\|A\mu - F\|^2$ over $\mu \in \mathcal{M}$, where $\|\cdot\|$ is the $L^2(\mathcal{C})-$norm, $F(s)$ is the the measured data, and $s \in \mathcal{C}$. The solution does

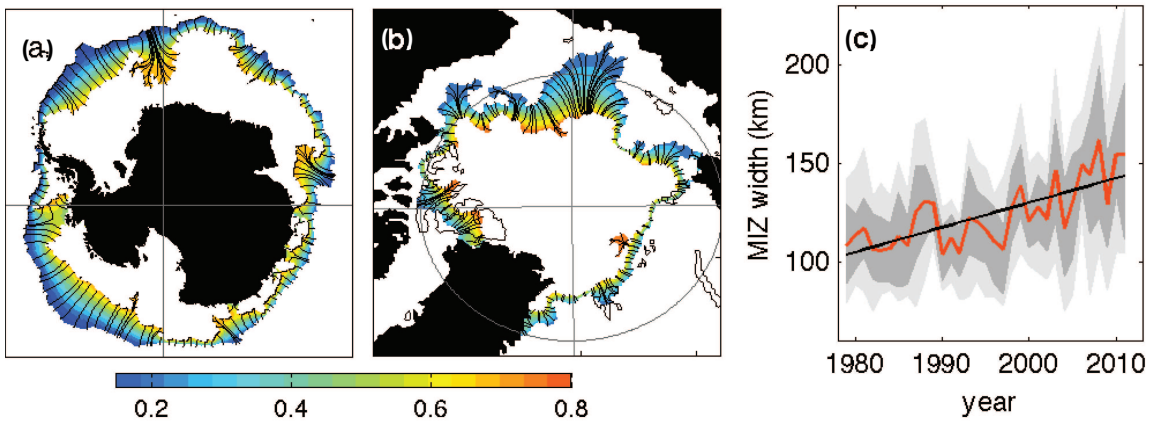

Figure 8: (a) Shading shows the solution to Laplace's equation within the Antarctic MIZ (ψ) on 26 August 2010, and black curves show MIZ width measurements following the gradient of ψ (only a subset shown for clarity). (b) Same as (a), but for the Arctic MIZ on 29 August 2010. (c) Width of the July-September MIZ for 1979-2011 (red curve). Percentiles of daily MIZ widths are shaded dark gray (25^{th} to 75^{th}) and light gray (10^{th} to 90^{th}). Results are based on analysis of satellite-derived sea ice concentrations from the National Snow and Ice Data Center.

not depend continuously on the data, and regularization based on constrained minimization is needed. Instead of minimizing $\|A\mu - F\|^2$ over all functions in $\mathcal{M}$, it is performed over a convex subset satisfying $J(\mu) \leq \beta$, for a stabilizing functional $J(\mu)$ and some $\beta > 0$. The advantage of using quadratic $J(\mu) = \|L\mu\|^2$, is the linearity of the corresponding Euler equation resulting in efficiency of the numerical schemes. However, the reconstructed solution necessarily possesses a certain smoothness. Nonquadratic stabilization imposes constraints on the variation of the solution. The total variation penalization, as well as a nonnegativity constraint, does not imply smoothness, permitting more general recovery, including the important Dirac measures.

We have also solved exactly a reduced inverse spectral problem by bounding the volume fraction of the constituents, an inclusion separation parameter q, and the spectral gap of $\Gamma\chi_1$. We developed an algorithm based on the Möbius transformation structure of the forward bounds whose output is a set of algebraic curves in parameter space bounding regions of admissible parameter values. These results advance the development of techniques for characterizing the microstructure of composite materials, and have been applied to sea ice to demonstrate electromagnetically that the brine inclusion separations vanish as the percolation threshold is approached.

5 Geometry of the Marginal Ice Zone

Dense pack ice transitions to open ocean over a region of broken ice termed the marginal ice zone (MIZ)—a highly dynamic region where the ice cover lies close to an open ocean boundary and intense atmosphere–ice–ocean interactions take place. The width of the MIZ is a fundamental length scale for polar dynamics in part because it represents the distance over which ocean waves and swell penetrate into the sea ice cover. Wave penetration can break a smooth ice layer into floes, meaning the MIZ acts as a buffer zone that protects the stable morphology of the inner ice. Waves also promote the formation of pancake ice, as shown in Figure 4. Moreover, the width of the MIZ is an important spatial dimension of the marine polar habitat and impacts human accessibility to high latitudes. Using a conformal mapping method to quantify MIZ width (see below), a dramatic 39% widening of the summer Arctic MIZ, based on three decades of satellite–derived data (1979-2012), was reported.

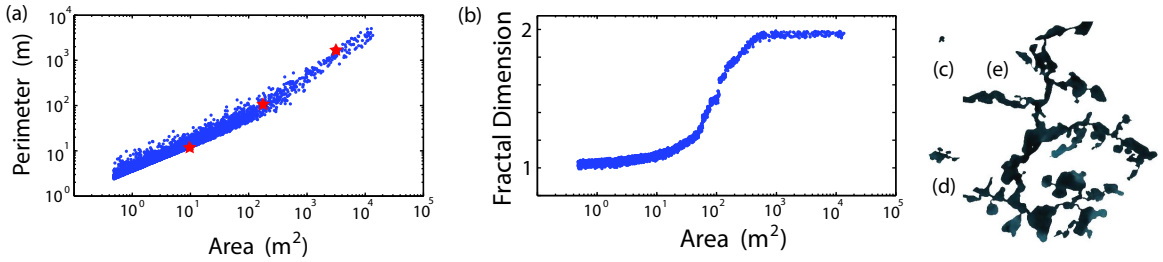

Figure 9: (a) Area–perimeter data for 5,269 Arctic melt ponds, plotted on logarithmic scales. The slope transitions from about 1 to 2 at a critical length scale of around 100 square meters. (b) Melt pond fractal dimension D as a function of area A, computed from the data in (a), showing the transition to complex ponds with increasing length scale. Ponds corresponding to the three red stars in (a), from left to right, are shown in (c), (d), and (e), respectively. The transitional pond in (d) has horizontal scale of about 30 m.

Challenges associated with objective measurement of the MIZ width include the MIZ shape, which is in general not geodesically convex, as illustrated by the example shaded white in Figure 8 (a). Sea ice concentration (c) is used here to define the MIZ as a body of marginal ice ($0.15 \leq c \leq 0.80$) adjoining both pack ice ($c > 0.80$) and sparse ice ($c < 0.15$). To define an objective MIZ width applicable to such shapes, an idealized sea ice concentration field $\psi(x, y)$ satisfying Laplace's equation within the MIZ,

$$\nabla^2 \psi = 0, \tag{17}$$

was introduced. We use (x, y) to denote a point in two dimensional space, and it is understood that we are working on the spherical Earth. Boundary conditions for (17) are $\psi = 0.15$ where MIZ borders a sparse ice region and $\psi = 0.80$ where the MIZ borders a pack ice region. The solutions to (17) for the examples in Figure 8 (a) and (b) are illustrated by color shading. Any curve γ orthogonal to the level curves of ψ and connecting two points on the MIZ perimeter (a black field line through the gradient field $\nabla\psi$ as in Figure 8 (b)) is contained in the MIZ, and its length provides an objective measure of MIZ width (ℓ). Defined in this way, ℓ is a function of distance along the MIZ perimeter (s) from an arbitrary starting point, and this dependence is denoted $\ell = \ell(s)$. Analogous applications of Laplace's equation have been introduced in medical imaging to measure the width or thickness of human organs.

Derivatives in (17) were numerically approximated using second-order finite differences, and solutions were obtained in the data's native stereographic projection since solutions of Laplace's equation are invariant under conformal mapping. For a given day and MIZ, a summary measure of MIZ width (w) can be defined by averaging ℓ with respect to distance along the MIZ perimeter:

$$w = \frac{1}{L_M} \int_M \ell(s)\, ds, \tag{18}$$

where M is the closed curve defining the MIZ perimeter and L_M is the length of M. Averaging w over July-September of each available year reveals the dramatic widening of the summer MIZ, as illustrated in Figure 8 (c).

6 Geometry of Arctic Melt Ponds

From the first appearance of visible pools of water, often in early June, the area fraction ϕ of sea ice covered by melt ponds can increase rapidly to over 70% in just a few days. Moreover, the accumulation of water at the surface dramatically lowers the albedo where the ponds form. There is a corresponding critical drop-off in average albedo. The resulting increase in solar absorption in the ice and upper ocean accelerates melting, possibly triggering *ice-albedo feedback*. Similarly, an increase in open water fraction lowers albedo, thus increasing solar absorption and subsequent melting. The spatial coverage and distribution of melt

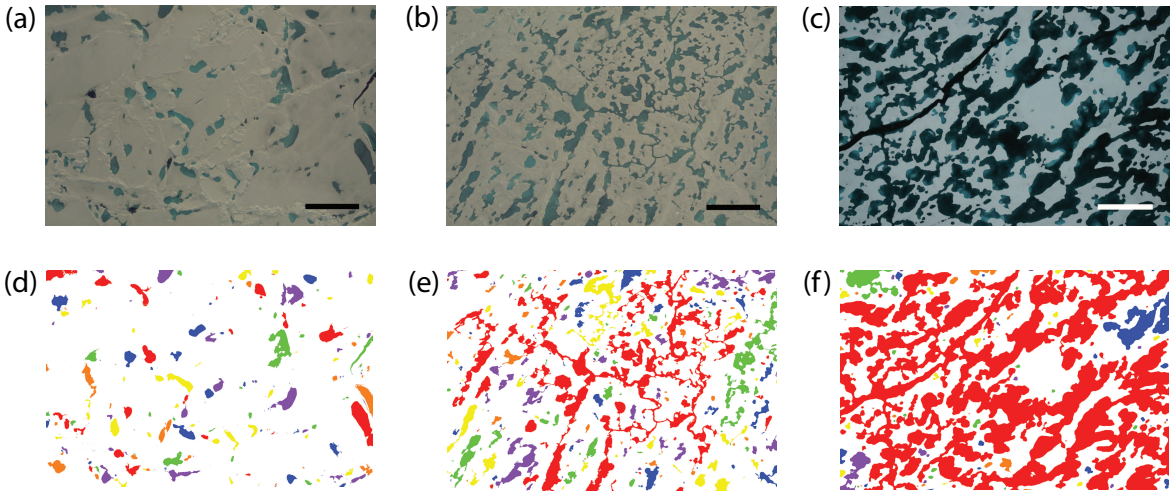

Figure 10: Evolution of melt pond connectivity and color coded connected components. (a) disconnected ponds, (b) transitional ponds, (c) fully connected melt ponds. The bottom row shows the color coded connected components for the corresponding image above: (d) no single color spans the image, (e) the red phase just spans the image, (f) the connected red phase dominates the image. The scale bars represent 200 meters for (a) and (b), and 35 meters for (c).

ponds on the surface of ice floes and the open water between the floes thus exerts primary control of ice pack albedo and the partitioning of solar energy in the ice-ocean system. Given the critical role of ice-albedo feedback in the recent losses of Arctic sea ice, ice pack albedo and the formation and evolution of melt ponds are of significant interest in climate modeling.

While melt ponds form a key component of the Arctic marine environment, comprehensive observations or theories of their formation, coverage, and evolution remain relatively sparse. Available observations of melt ponds show that their areal coverage is highly variable, particularly for first year ice early in the melt season, with rates of change as high as 35% per day. Such variability, as well as the influence of many competing factors controlling melt pond and ice floe evolution, makes the incorporation of realistic treatments of albedo into climate models quite challenging. Small and medium scale models of melt ponds which include some of these mechanisms have been developed, and melt pond parameterizations are being incorporated into global climate models.

The surface of an ice floe is viewed here as a two phase composite of dark melt ponds and white snow or ice. The onset of ponding and the rapid increase in coverage beyond the initial threshold is similar to critical phenomena in statistical physics and composite materials. It is natural, therefore, to ask if the evolution of melt pond geometry exhibits universal characteristics that do not necessarily depend on the details of the driving mechanisms in numerical melt pond models. Fundamentally, the melting of Arctic sea ice is a phase transition phenomenon, where a solid turns to liquid, albeit on large regional scales and over a period of time which depends on environmental forcing and other factors. We thus look for features of melt pond evolution that are mathematically analogous to related phenomena in the theories of phase transitions and composite materials. As a first step in this direction, we consider the evolution of geometric complexity of Arctic melt ponds.

By analyzing area−perimeter data from hundreds of thousands of melt ponds, we have discovered an unexpected separation of scales, where the pond fractal dimension D exhibits a transition from 1 to 2 around a critical length scale of 100 square meters in area, as shown in Fig-

ure 9. Small ponds with simple boundaries coalesce or percolate to form larger connected regions. Pond complexity increases rapidly through the transition region and reaches a maximum for ponds larger than 1000 m^2 whose boundaries resemble space filling curves with $D \approx 2$. These configurations affect the complex radiation fields under melting sea ice, the heat balance of sea ice and the upper ocean, under-ice phytoplankton blooms, biological productivity, and biogeochemical processes.

Melt pond evolution also appears to exhibit a *percolation threshold*, where one phase in a composite becomes connected on macroscopic scales as some parameter exceeds a critical value. An important example of this phenomenon in the microphysics of sea ice (discussed above), which is fundamental to the process of melt pond drainage, is the percolation transition exhibited by the brine phase in sea ice, or the *rule of fives* discussed in section 4.1. When the brine volume fraction of columnar sea ice exceeds about 5%, the brine phase becomes macroscopically connected so that fluid pathways allow flow through the porous microstructure of the ice. Similarly, even casual inspection of the aerial photos in Figure 10, shows that the melt pond phase of sea ice undergoes a percolation transition where disconnected ponds evolve into much larger scale connected structures with complex boundaries. Connectivity of melt ponds promotes further melting and break-up of floes, as well as horizontal transport of meltwater and drainage through cracks, leads, and seal holes.

Further Reading

1. Avellaneda, M. and A. Majda. 1989, Stieltjes integral representation and effective diffusivity bounds for turbulent transport. *Phys. Rev. Lett.* 62:753–755.
2. Bergman, D. J. and D. Stroud. 1992, Physical properties of macroscopically inhomogeneous media. *Solid State Phys.* 46:147–269.
3. Cherkaev, E. 2001, Inverse homogenization for evaluation of effective properties of a mixture. *Inverse Problems* 17:1203–1218.
4. Eisenman, I. and J. S. Wettlaufer. 2009, Nonlinear threshold behavior during the loss of Arctic sea ice. *Proc. Natl. Acad. Sci.* 106(1):28–32.
5. Feltham, D. L. 2008, Sea ice rheology. *Ann. Rev. Fluid Mech.* 40:91–112.
6. Flocco, D., D. L. Feltham, and A. K. Turner. 2010, Incorporation of a physically based melt pond scheme into the sea ice component of a climate model. *J. Geophys. Res.* 115:C08,012 (14 pp.), doi:10.1029/2009JC005,568.
7. Golden, K. M. 2009, Climate change and the mathematics of transport in sea ice. *Notices of the American Mathematical Society* 56(5):562–584 and issue cover.
8. Hohenegger, C., B. Alali, K. R. Steffen, D. K. Perovich, and K. M. Golden. 2012, Transition in the fractal geometry of Arctic melt ponds. *The Cryosphere* 6:1157–1162.
9. Hunke, E. C. and W. H. Lipscomb. 2010, CICE: the Los Alamos Sea Ice Model Documentation and Software Users Manual Version 4.1 LA-CC-06-012, t-3 Fluid Dynamics Group, Los Alamos National Laboratory.
10. Milton, G. W. 2002, *Theory of Composites.* Cambridge: Cambridge University Press.
11. Orum, C., E. Cherkaev, and K. M. Golden. 2011, Recovery of inclusion separations in strongly heterogeneous composites from effective property measurements. *Proc. Roy. Soc. London A* pp. doi:10.1098/rspa.2011.0527, pp. 1–27, online November 16.
12. Perovich, D. K., J. A. Richter-Menge, K. F. Jones, and B. Light. 2008, Sunlight, water, and ice: Extreme Arctic sea ice melt during the summer of 2007. *Geophys. Res. Lett.* 35:L11,501, doi:10.1029/2008GL034,007.
13. Stauffer, D. and A. Aharony. 1992, *Introduction to Percolation Theory, Second Edition.* London: Taylor and Francis Ltd.
14. Stroeve, J., M. M. Holland, W. Meier, T. Scambos, and M. Serreze. 2007, 2007: Arctic sea ice decline: Faster than forecast. *Geophys. Res. Lett.* 34:L09,591, doi: 10.1029/2007GL029,703.
15. Strong, C. and I. G. Rigor. 2013, Arctic marginal ice zone trending wider in summer and narrower in winter. *Geophys. Res. Lett.* 40(18):4864–4868.
16. Thomas, D. N. and G. S. Dieckmann, editors. 2009, *Sea Ice, 2nd Edition.* Oxford: Wiley-Blackwell.
17. Thompson, C. J. 1988, *Classical Equilibrium Statistical Mechanics.* Oxford: Oxford University Press.
18. Torquato, S. 2002, *Random Heterogeneous Materials: Microstructure and Macroscopic Properties.* New York: Springer-Verlag.
19. Untersteiner, N. 1986, *The Geophysics of Sea Ice.* New York: Plenum.
20. Washington, W. and C. L. Parkinson. 2005, *An Introduction to Three-Dimensional Climate Modeling, 2nd Edition.* Herndon, VA: University Science Books.